Journal of
Computational and Theoretical Nanoscience
Vol. 3, 1–14, 2006

Buckling, Bundling, and Pattern Formation: From Semi-Flexible Polymers to Assemblies of Interacting Filaments

Jan Kierfeld*, Petra Gutjahr, Torsten Kühne, Pavel Kraikivski, and Reinhard Lipowsky

Max Planck Institute of Colloids and Interfaces, Science Park Golm, 14424 Potsdam, Germany

Semiflexible polymers and filaments play an important role in biological and chemical physics. Single filaments are characterized by a certain bending rigidity which governs their persistence length and buckling instabilities. Attractive mutual interactions of filaments in bundles or the attractive interaction with an adhesive substrate lead to equilibrium phase transitions, such as bundling and adsorption. Finally, on the level of active systems consisting of many interacting filaments, we discuss cooperative ordering effects in non-equilibrium systems such as motility assays. In motility assays filaments are adsorbed and driven by motor proteins, which are anchored to a planar two-dimensional substrate. The interaction with motor proteins leads to enhanced ordering of filaments. Motility assays containing patterns of adsorbed motors, i.e., stripes of low motor density with increasing widths can be used to sort filaments according to their lengths.

Keywords: Filaments, Semiflexible Polymers, Molecular Motors, Buckling, Bundling, Pattern Formation.

RESEARCH ARTICLE

1. INTRODUCTION

Stiff, filamentous polymers play an important role in biological and chemical physics. Both DNA or cytoskeletal filaments such as F-actin and microtubules[1,2] and chemically synthesized stiff polymers such as dendronized polymers[3] are "nanorods." These polymers have diameters in the range from 2 to 25 nanometers which leads to a considerable bending rigidity and gives rise to persistence lengths comparable to or larger than the polymer's contour lengths. Such semiflexible polymers exhibit a variety of cooperative phenomena, which we will briefly review in this article. The cooperative behavior arises from the competition of several energies in the system, i.e., the bending energy, the thermal energy, interaction energies, and external driving forces. In biological systems, driving forces can arise from the activity of molecular motors which perform directed motion on cytoskeletal filaments or the polymerization dynamics of cytoskeletal filaments. Both the activity of molecular motors and the polymerization dynamics are processes far from equilibrium and are typically coupled to the hydrolysis of adenine triphosphate (ATP).

First, we will consider two aspects of single filaments related to the cooperative behavior of their bending modes, the renormalization of bending rigidity and the buckling instability. The bending rigidity renormalization leads to an effective softening of large-scale fluctuations of a filament, which can be quantified using renormalization group methods.[4] The buckling instability is an important effect that restricts the force generation by growing filaments. We discuss a cusp-like singularity in the projected length as a function of the filament length, which can serve as an experimental signature for the buckling of growing filaments or rods.

Then we will discuss the equilibrium phase transition that leads to the formation of filament bundles in the presence of attractive interactions, which can arise from crosslinking proteins or unspecific interactions.[5] In eukaryotic cells, the most important building blocks of the cytoskeleton are microtubules and filamentous actin (F-actin). Actin filaments have a persistence length $L_p \simeq 30\ \mu$m,[6] microtubules are much stiffer with a persistence length $L_p \simeq 10$ mm.[7] In the cortex of the cell, actin filaments form a dense meshwork which is responsible for many of the viscoelastic properties of the cell. Another important morphology that is found in the cell are filament bundles,[8] which, e.g., support cell protrusions and serve as stress fibres. Both meshworks and bundles are hold together by different actin-binding crosslinking proteins.[8,9] Actin bundling crosslinkers possess two adhesive end domains

*Author to whom correspondence should be addressed.

which bind to filaments by weak bonds; crosslinker mediated interactions therefore allow a reversible formation of actin bundles, which can be regulated by the concentration of crosslinkers in solution. Solution of actin filaments and crosslinking proteins have been studied *in vitro* in a number of recent experiments.[10–12] In these studies it has been observed that bundle formation in F-actin solutions containing crosslinking molecules requires a threshold crosslinker concentration above which (i) F-actin bundles become stable against the thermal fluctuations of filaments and (ii) a phase containing networks of bundles separates. Polymerizing bundles are used within the cell in order to generate forces.[13, 14] We will shortly discuss one possible "zipping"-mechanism for force generation which is based on the conversion of adhesive energy into polymerizing forces.

Another important equilibrium phase transition of polymers is their adsorption to an attractive planar surface. For semiflexible polymers or filaments, the adsorption transition is similar to the binding of two filaments but represents a distinct universality class.[15] Various single molecule methods have been applied to adsorbed semiflexible polymers because both visualization and manipulation are easier for adsorbed polymers with a large diameter, such as DNA.[16, 17] These polymers are generically semiflexible because strong entropic or enthalpic interactions along their backbone increase the bending rigidity. The manipulation kinetics of strongly adsorbed single filaments or semiflexible polymers on structured substrates requires thermal activation.[18, 19] Here, we will discuss the adsorption behavior of filaments in motility assays. In such an assay, cytoskeletal filaments are adsorbed and driven over a two-dimensional, planar substrate by motor proteins whose tails are anchored to the substrate.[20] In order to obtain adsorption, a critical density of motor proteins is needed in close analogy to the critical crosslinker concentration for the formation of a filament bundle.

Motility or gliding assays are a standard biochemistry assay to characterize motor proteins, which is based on measuring the lateral displacement of adsorbed filaments. In biological cells, small forces generated by motor proteins organize and rearrange cytoskeletal filaments and give rise to active, non-equilibrium filament dynamics, which plays an important role for cell division, motility, and force generation.[1, 2] Whereas conventional "passive" polymer dynamics is governed by thermal fluctuations,[21] active filament dynamics is characterized by a constant supply of mechanical energy by motor proteins, which hydrolyze ATP. Motility assays are model systems, which allow to study active filament dynamics in a controlled manner. By analyzing the transport velocities of *single* filaments gliding over the substrate, information can be obtained about basic properties of molecular motors such as their maximal velocity. We introduce a simulation model for motility assays, which refines previous models[22–24] and contains semiflexible filaments, motor heads, and polymeric motor tails as separate degrees of freedom.

In such motility assays, several interesting ordering phenomena can occur on the nanoscale if we consider *many* interacting filaments. The ordering is caused by the interplay of the active dynamics of filaments and their mutual repulsive interactions. On the one hand, we find an increased tendency for nematic ordering in motility assays with *randomly* adsorbed motor proteins.[25] On the other hand, stripe-shaped *patterns* of adsorbed motors can be used for the length sorting or fractionation of filaments.

This article is organized as follows. In Section 2, the persistence length of a single filament is discussed in the framework of a systematic renormalization group approach. In Section 3, we discuss a particular feature of the buckling instability of a single filament, which is relevant to experiments on growing filaments. In Section 4, the formation of filament bundles via crosslinker-mediated attractive interactions and the ability of "zipping" bundles to generate forces is discussed. The adsorption of a filament on an adhesive surface, which is provided by a planar two-dimensional substrate covered with anchored motor proteins and which represents the geometry used in motility assays, is considered in Section 5. In Section 6, we introduce a model for the active filament dynamics in motility assays and present recent simulation results. These results demonstrate an enhanced nematic ordering of interacting filaments in motility assay. They also demonstrate that filaments can be sorted according to their length if striped patterns of different motor density are realized in a motility assay.

2. PERSISTENCE LENGTH

The coupling between the different bending modes of single filaments can lead to a considerable softening of the filaments on large length scales. On length scales larger than the persistence length L_p, the polymer appears to be flexible. We have quantified this effect using renormalization group (RG) methods; here we briefly summarize some of the results, details are presented elsewhere.[4] Starting from a discretized model for an inextensible semiflexible chain consisting of M bonds or segments of length ℓ_b and with unit tangent vectors $\mathbf{t}_i$ $(i = 1, \ldots, M)$ in d spatial dimensions. The bending energy of this semiflexible chain is given by[26]

$$\mathcal{H}\{\mathbf{t}_i\} = \frac{\kappa}{\ell_b} \sum_{i=1}^{M} (1 - \mathbf{t}_i \cdot \mathbf{t}_{i-1}), \quad \text{with } \mathbf{t}_i^2 = 1 \qquad (1)$$

where κ is the bending rigidity. Physically relevant cases are chains in three spatial dimensions ($d = 3$) and chains, which are adsorbed on a planar substrate and, thus, confined to two dimensions ($d = 2$). In the continuum limit of small ℓ_b the model (1) reduces to the continuous wormlike chain model for an inextensible filament.[27]

The partition sum is obtained by integrating over all possible bond orientations with the appropriate Boltzmann weight $\exp(-\mathcal{H}\{\mathbf{t}_i\}/T)$, where T is the temperature in energy units. Within the model (1), modes of different wavelengths are coupled. Upon integrating out short-scale fluctuations, this leads to a softening of the effective renormalized $\kappa(\ell)$ governing the fluctuations with wave length ℓ such that $\kappa(\ell) < \kappa$. In order to calculate $\kappa(\ell)$, we use a real-space functional renormalization group (RG) approach, which has been developed originally in the context of one-dimensional classical Heisenberg spin models.[28] The RG transformation eliminates fluctuations up to the scale $\ell = 2^R \ell_b$. After the Rth RG step, we can find an exact recursion relation for $\kappa_M = \kappa(2^R \ell_b)$. For $d = 2$, the resulting recursion relations are given by[4]

$$\frac{\kappa_R}{\kappa} = \frac{2^R}{K_0} \left\{ \sum_{m=-\infty}^{\infty} [\lambda_m^{(0)}(K_0)]^{2^R} m^2 \right\} \Big/ \left\{ \sum_{m=-\infty}^{\infty} [\lambda_m^{(0)}(K_0)]^{2^R} \right\}$$
$$\text{with } K_0 \equiv \kappa/\ell_b T \quad \text{and} \quad \lambda_m^{(0)}(K_0) \equiv e^{-K_0} I_m(K_0) \tag{2}$$

where $I_m(x)$ denotes the modified Bessel function of the first kind.[29] A similar recursion relation can be found for $d = 3$. The renormalized $\kappa(\ell)$ for $d = 2$ and $d = 3$ is plotted in Figure 1 as a function of the length scale ℓ. For large ℓ, the expression (2) has the asymptotic behavior

$$\frac{\kappa(\ell)}{\kappa} \approx \ell \frac{T}{\kappa} (2e^{-\ell T/2\kappa} - 4e^{-\ell T/\kappa} + 8e^{-3\ell T/2\kappa} - \cdots) \tag{3}$$

which is governed, to leading order, by the decay length $L_p = 2\kappa/T$ which we identify with the persistence length in $d = 2$. Similarly, we define $L_p = \kappa/T$ in $d = 3$. These results generalize the conventional definitions based on the exponential decay of the particular two-point tangent correlation function and gives identical results for L_p. In the remainder of this article we will define the persistence length by the $d = 2$ result, i.e.,

$$L_p \equiv 2\kappa/T \tag{4}$$

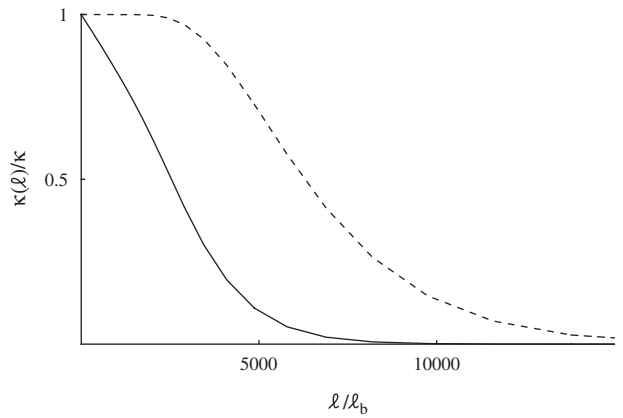

Fig. 1. $\kappa(\ell)/\kappa$ as a function of $\ell/\ell_b = 2^R$ for $K_0 = 1000$ for $d = 2$ (dashed line) according to the recursion relation (2 and $d = 3$ (solid line)).

3. BUCKLING INSTABILITY

Another hallmark of filaments or nanorods with bending elasticity is the presence of buckling instabilities if the filament is subject to a large compressional force of size F as follows from classical elasticity theory.[30] In the absence of thermal fluctuations, the filament undergoes such an instability if the compressional force F exceeds a certain threshold value, the critical force F_c, for constant filament length or if the filament length L exceeds a certain critical length L_c for constant force. We will limit our discussion to the situation of a longitudinal force F that acts parallel to the straight, unbuckled state of the filament. The threshold values for force and filament length are then given by

$$F_c = c_{bc}^2 \pi^2 \kappa / L^2 \quad \text{and} \quad L_c = c_{bc} \pi (\kappa/F)^{1/2} \tag{5}$$

where c_{bc} is a dimensionless coefficient that depends on the boundary conditions at the two filament ends. For the three boundary conditions (bc0), (bc1), and (bc2) described in the next paragraph and illustrated in Figure 2, one has $c_{bc} = 1/2$, 1, and 2, respectively.

Let us denote the two ends of the filament by e_1 and e_2. Filament end e_1 is taken to be immobilized and to have a fixed spatial position. The orientation of the filament segment adjacent to e_1, which is described by the tangent vector of this segment, may be free or clamped: 'free' means that it can freely adapt to the compressional force, 'clamped' that it is constrained to be parallel to this force. The three boundary conditions are now defined as follows (see also Fig. 2): (bc0) Filament end e_1 is clamped and filament end e_2 is free. In this case, a longitudinal force that acts parallel to the straight, unbuckled filament leads to a displacement of e_2 that has both a longitudinal and a transverse component; (bc1) Both filament ends are free. As the filament buckles, the filament end e_2 is only displaced in the longitudinal direction parallel to the force; and (bc2) Both filament ends are clamped and we only

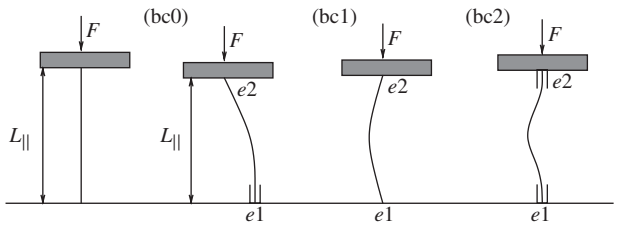

Fig. 2. Straight unbuckled filament and three boundary conditions (bc0), (bc1), and (bc2) for buckling. (Left) Straight, unbuckled filament growing against the upper (grey) wall which exerts the longitudinal force F. The projected length $L_\parallel$ of the filament is equal to its contour length L. The straight filament is stable as long as L do not exceed a critical value L_c, which differs for the three boundary conditions (bc0), (bc1), and (bc2), see Eq. (5). For $L > L_c$ the filament buckles and $L_\parallel < L$. The lower filament end $e1$ has a fixed spatial position. For (bc0), filament end $e1$ is clamped to an orientation parallel to the force and filament end $e2$ is free; for (bc1), both filaments ends can freely adapt their orientations; for (bc2), both filament ends have clamped orientation and, furthermore, we only allow for displacements of $e2$ parallel to the force.

RESEARCH ARTICLE

allow for a longitudinal displacement of e_2 parallel to the force.

In the living cell, the ATP-driven polymerization of filaments is an important mechanism for force generation. Likewise, synthetic semiflexible polymers, which grow via polymerization, can be envisaged as suitable systems for force generation on the nanoscale. The ability of these systems to perform work is, however, limited by the buckling instability. Here we want to discuss a simple model system where a single filament is growing by polymerization against a planar wall. As before, one filament end, e_1, is immobilized and has a fixed spatial position. The other end, e_2, can now grow by attachment of monomers which leads to a time-dependent filament length $L = L(t)$. Since this growth is rather slow, we can assume that the filament attains a state of mechanical equilibrium with length $L = L(t)$. The planar wall is movable and is loaded by a constant force F, such that it always touches and pushes the growing end of the filament. Now we investigate how the buckling instability of the filament is reflected in the behavior of the projected length $L_\parallel$, which is the longitudinal extension of the filament in the direction parallel to the force and is directly accessible in experiments.

If the filament bends in a plane, its configuration can be described by the planar angle $\phi(s)$ between its tangent vector and the force direction which is parametrized by the arc length s with $0 < s < L$. The total energy E of the filament then has the form

$$E = \int_0^L ds \left[\frac{\kappa}{2} (\partial_s \phi) 2 + F \cos \phi(s) \right] \tag{6}$$

where the first and the second term represent the bending and compression energy, respectively. The force F is positive if it acts against the growing filament. The projected length $L_\parallel$ is given by

$$L_\parallel = \int_0^L ds \cos \phi(s) \tag{7}$$

Minimizing the total energy E with respect to the angle configuration $\phi(s)$, leads to the beam equation which has to be solved for appropriate boundary conditions. This solution can be expressed in terms of the planar angle $\phi_* \equiv \phi(s_*)$. For the boundary conditions (bc0) and (bc1), one simply has $s_* = L$. For the boundary condition (bc2), the arc length s_* corresponds to the smallest s-value for which the filament's curvature vanishes which implies $d\phi(s)/ds = 0$ for $s = s_*$. One then finds that the ratios of the contour length L and of the projected length $L_\parallel$ to the critical length L_c are given by

$$\frac{L}{L_c} = \frac{\mathcal{J}_1(\phi_*)}{\mathcal{J}_1(0)} \quad \text{and} \quad \frac{L_\parallel}{L_c} = \frac{\mathcal{J}_1(\phi_*) - \mathcal{J}_2(\phi_*)}{\mathcal{J}_1(0)} \tag{8}$$

with the two integrals

$$\mathcal{J}_1(y) \equiv \int_0^y dx \frac{1}{\sqrt{2(\cos x - \cos y)}} \tag{9}$$

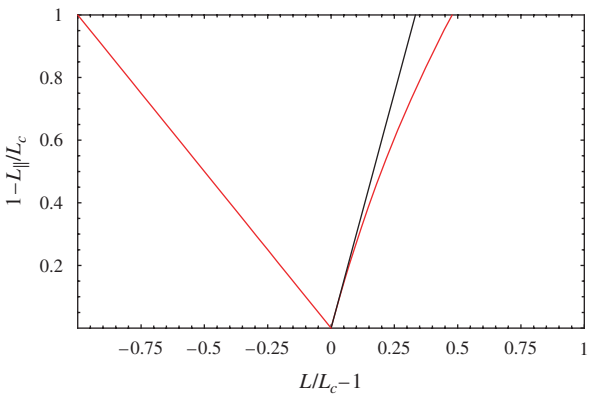

Fig. 3. Plot of the reduced projected length $L_\parallel/L_c$ as a function of the reduced contour length L/L_c for the two boundary conditions (bc0) and (bc1), see text. For $L < L_c$, the filament is straight with $L_\parallel = L$ which corresponds to the left part of the diagram with $L/L_c - 1 < 0$. The buckled solution appears for $L > L_c$ as shown in the right part of the diagram with $L/L_c - 1 > 0$. The red curve is obtained numerically by a parametric plot using $\phi_* = \phi(L)$ as the curve parameter. The black line is the linear approximation (11). For $L/L_c - 1 > 0.478$, $L_\parallel$ becomes negative.

and

$$\mathcal{J}_2(y) \equiv \int_0^y dx \frac{1 - \cos x}{\sqrt{2(\cos x - \cos y)}} \tag{10}$$

As y goes to zero, the first integral has the finite limit $\mathcal{J}_1(0) = \pi/2$ whereas $\mathcal{J}_2(0) = 0$. Using these expressions, one can obtain a parametric representation of the reduced projected length $L_\parallel/L_c$ as a function of the reduced contour length L/L_c in the buckled state with $L > L_c$. For the two boundary conditions (bc0) and (bc1), one obtains the same relation which is plotted in Figure 3. Close to the buckling instability, all three boundary conditions lead to the asymptotic behavior

$$1 - L_\parallel/L_c \approx 3(L/L_c - 1) \quad \text{for small } L/L_c - 1 > 0 \tag{11}$$

For $L < L_c$, on the other hand, the filament is unbuckled which implies that the projected length $L_\parallel$ is identical with the contour length L and

$$1 - L_\parallel/L_c = 1 - L/L_c \quad \text{for } L/L_c - 1 < 0 \tag{12}$$

Combining the two results for $L > L_c$ and $L < L_c$, we see that the relation between projected and contour length exhibits a cusp at the buckling point with $L = L_c$ as shown in Figure 3.

For a growing filament this cusp-like singularity directly translates into a singularity in time. The filament growth can be characterized by the rate $\omega_{\text{eff}}(F)$ of subunit insertion or attachment which depends on the external force F. The time-dependent length of the filament is then given by

$$L(t) = L_c + \ell_b \, \omega_{\text{eff}}(F)(t - t_c) \tag{13}$$

where ℓ_b is the size of the inserted subunits and t_c is the buckling time. As an example, let us consider an actin filament which is extended by a formin molecule with insertion rate $\omega_{\text{eff}}(0) \simeq 2.5$ subunits/s and subunit size

$\ell_b \simeq 2.75$ nm.[31] Using the growth law (13) for $L(t)$ in (11) for $t > t_c$ and in (12) for $t < t_c$, one obtains the jump

$$\left.\frac{dL_\parallel}{dt}\right|_{t=t_c+0} - \left.\frac{dL_\parallel}{dt}\right|_{t=t_c-0} = -4\,\ell_b\,\omega_{\rm eff}(F) \qquad (14)$$

in the growth rate $dL_\parallel/dt$ of the projected length at the buckling instability. This singularity should be accessible to experiments and can then be used to determine the growth rate $\omega_{\rm eff}(F)$ of the filament or nanorod. The singularity as given by (14) also applies to N parallel filaments provided one replaces F by F/N.

4. FILAMENT BUNDLES

Within this section we consider an equilibrium phase transition in a system of *many* filaments, which have a short-range attractive interaction mediated by crosslinkers. We consider N filaments with bending rigidity κ in a solution containing crosslinking molecules with two adhesive end groups. This system exhibits a critical crosslinker concentration, $X_1 = X_{1,c}$, which separates two different concentration regimes. For $X_1 < X_{1,c}$, the filaments are unbound and uniformly distributed within the compartment. For $X_1 > X_{1,c}$, the filaments form either a single bundle, which represents the true ground state of the system as in Figures 4(a) and (c), or several sub-bundles, which represent metastable, kinetically trapped states as in Figure 4(b). Furthermore, as we decrease the crosslinker concentration from a value above $X_{1,c}$ towards a value below $X_{1,c}$, the bundles undergo a discontinuous unbinding transition at $X_1 = X_{1,c}$. The existence of a single, discontinuous unbundling transition can be established by analytic methods for $N = 2$ filaments[15] and by Monte Carlo (MC) simulations for larger bundles containing up to $N = 20$ filaments.[5]

4.1. Model

The filaments are oriented along one axis, say the x-axis, and can be parametrized by two-dimensional displacements $\mathbf{z}_i(x)$ $(i = 1, \ldots, N)$ perpendicular to the x-axis,

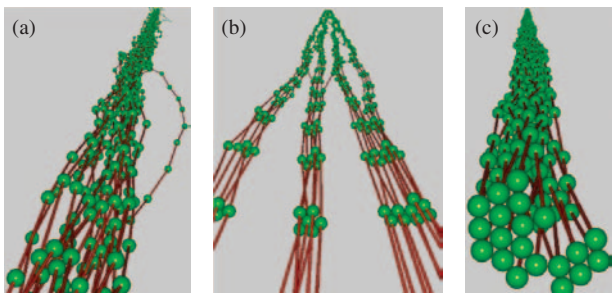

Fig. 4. Monte Carlo snapshots of bundles with $N = 20$ filaments. (a) Close to the unbinding transition in the bundled phase. (b) Deep in the bound phase, the bundle tends to segregate due to slow kinetics and filament entanglement. (c) The equilibrium shape of the bundle is roughly cylindrical.

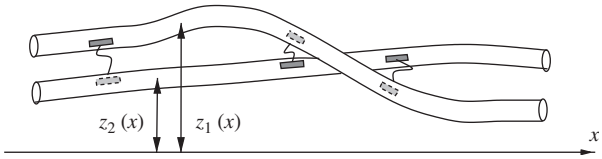

Fig. 5. Crosslinkers connecting two filaments. If these crosslinker molecules are rather rigid, they mediate effective filament–filament interactions that depend on the filament orientations as discussed in Ref. [15]. In this review, we will focus on the case of short, flexible crosslinkers with two adhesive endgroups as indicated in this figure. In the latter case, the effective filament–filament interactions depend only on the distance between the filaments.

with $0 < x < L_\parallel$, where $L_\parallel$ is the projected length of the polymer. This parametrization is appropriate provided the longitudinal correlation length of the displacements is small compared to $L_{\rm p}$. The filament interaction is mediated by crosslinking sticker molecules that adsorb from the surrounding solution. Each linker consists of a short polymer with adhesive endgroups, see Figure 5. In the following, we assume flexible linkers for simplicity which can link two filaments irrespective of their orientation; orientation-dependent interactions which arise from rigid linkers can be studied in a similar way, see Ref. [15].

We discretize the filament into segments of length $a_\parallel$, i.e., $x_k = k a_\parallel$ and $\mathbf{z}_{i,k} = \mathbf{z}_i(x_k)$. The presence or absence of a crosslinker molecule at segment k of filament i is described by the occupation number $n_{i,k} = n_i(x_k) = 0, 1$. The filament-crosslinker system is governed by the Hamiltonian

$$\mathcal{H} = \sum_i [\mathcal{H}_{b,i}\{\mathbf{z}_i\} + \mathcal{H}_1\{n_i\}] + \sum_{i,j} \mathcal{H}_2\{\mathbf{z}_i - \mathbf{z}_j, n_i, n_j\} \quad (15)$$

where the first contribution

$$\mathcal{H}_{b,i} = \int_0^L dx \frac{1}{2}\kappa(\partial_x^2 \mathbf{z}_i)^2$$

contains the bending energies of the filaments. The term $\mathcal{H}_1$ describes the intrafilament interactions of linkers. We consider a lattice gas of linkers with hard-core repulsion adsorbing on a filament with

$$\mathcal{H}_1 = \sum_k a_\parallel W n_{i,k}$$

where $W < 0$ is the adhesive energy (per length) of one linker end group. The third contribution $\mathcal{H}_2$ describes the pairwise interactions between filaments i and j and is given by

$$\mathcal{H}_2 = \sum_k a_\parallel \left[V_r(\Delta\mathbf{z}_{ij,k}) + \frac{1}{2}(n_{i,k} + n_{j,k} - 2n_{i,k}n_{j,k}) V_a(\Delta\mathbf{z}_{ij,k}) \right] \quad (16)$$

where $\Delta\mathbf{z}_{ij,k} \equiv \mathbf{z}_{i,k} - \mathbf{z}_{j,k}$. The first term represents the hard-core repulsion between two filaments that is independent of the linker occupation and leads to a potential

$$V_r(\mathbf{z}) = \infty \quad \text{for } |\mathbf{z}| < \ell_r \quad \text{and} \quad V_r(\mathbf{z}) = 0 \text{ otherwise}$$

The length scale ℓ_r is of the order of the filament diameter. The second term is the linker-mediated attraction and is

RESEARCH ARTICLE

non-zero if either segment k of filament i or segment k of filament j carries a linker. Then the other filament is attracted by a linker-mediated potential $V_a(\mathbf{z})$. The latter filament gains the additional energy $|W|$ if $|\Delta\mathbf{z}_{ij,k}| \leq \ell_a$, where the potential range ℓ_a is of the order of the linker size. This attraction is modeled by the potential well

$$V_a(\mathbf{z}) = W \quad \text{for } 0 < |\mathbf{z}| - \ell_r < \ell_a \quad \text{and} \quad V_a(\mathbf{z}) = 0 \text{ otherwise} \tag{17}$$

We can perform the partial trace over the crosslinker degrees of freedom $n_{i,k}$ in the grand-canonical ensemble to obtain an effective interaction between filaments. Each crosslinker has two adhesive ends. The first adhesive end adsorbs on a filament and establishes the standard Langmuir-type adsorption equilibrium with a linker concentration per site $X_1 \equiv \langle n_{i,k}\rangle_1 = c_x/(K_d + c_x)$ where the average is taken with the Hamiltonian $\mathcal{H}_1$. X_1 is thus determined by the concentration c_x of linkers in solution, where K_d is the equilibrium constant of the dissociation reaction of the crosslinker with the filament. Tracing over weakly bound linkers with $|W| \ll T/a_\parallel$, we end up with effective pairwise linker-mediated filament interactions, i.e.,

$$\bar{\mathcal{H}}_2 \approx \frac{1}{2}\sum_k a_\parallel [V_r(\Delta\mathbf{z}_{ij,k}) + \bar{V}_a(\Delta\mathbf{z}_{ij,k})]$$

which have the same functional form as the bare interactions; the short-range attractive part $\bar{V}_a$ is of the form (17) with a strength[†]

$$\bar{W} \approx 2X_1 W \tag{18}$$

proportional to the linker concentration on the filament. Pairwise filament interactions with potentials of the form (17) are generic and do not only arise from crosslinkers but also from van-der-Waals, electrostatic, or depletion forces.

4.2. Discontinuous Unbundling Transition

We have studied bundle formation by MC simulations for up to $N = 20$ identical filaments ($\kappa_i = \kappa$) using the effective Hamiltonian

$$\mathcal{H} = \sum_i \mathcal{H}_{b,i} + \sum_{i,j} \bar{\mathcal{H}}_2$$

Filaments are discretized into $L_\parallel/\Delta x$ points along the x-direction, in which we apply periodic boundary conditions. In each MC step we attempt a random perpendicular displacement in the z-direction. The MC simulations can be used to determine the locus and order of the unbinding transitions, at which the mean energy $\langle\mathcal{H}\rangle$ exhibits a discontinuity, see Figure 6(a). To gain further insight into bundle morphologies, we also measure the mean segment separation $\langle|\Delta\mathbf{z}_{ij}| - \ell_r\rangle$, see Figure 6(b), which is

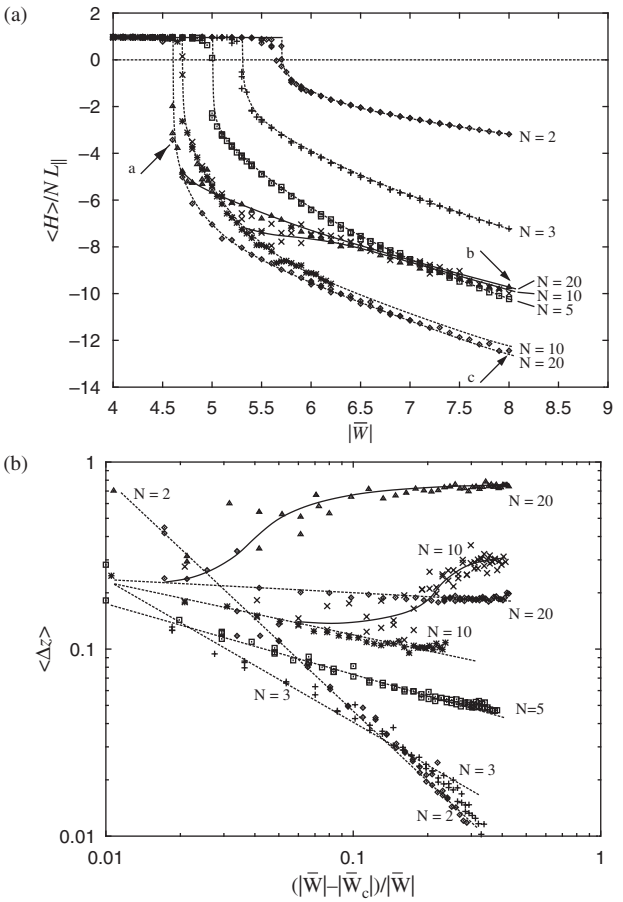

Fig. 6. MC data for $N = 2, 3, 5, 10, 20$ identical filaments (with persistence length $L_\mathrm{p} = 200$, contour length $L_\parallel = 100$, potential range $\ell_a = 0.001$, and hard core radius $\ell_r = 0.1$; all lengths are in units of Δx, lines are guides to the eye). For $N = 10, 20$ two branches of data are shown corresponding to two different initial conditions; in the lower branch we prepared a compact cylindrical configuration, in the upper branch (thick lines) we arranged filaments initially in a plane. (a) Mean energy $\langle\mathcal{H}\rangle/NL_\parallel$ per filament (in units of T) as a function of the effective potential strength $|\bar{W}|$ (in units of $T/\Delta x$). Arrows correspond to the snapshots in Figure 4. (b) Logarithmic plot of the mean filament separation $\langle\Delta z\rangle \equiv \langle|\Delta\mathbf{z}_{ij}| - \ell_r\rangle$ (in units of Δx) as a function of the reduced potential strength $(|\bar{W}| - |\bar{W}_c|)/|\bar{W}|$.

directly proportional to the mean bundle thickness that can be determined by optical microscopy in experiments.

Our MC simulations confirm that, for bundles containing up to $N = 20$ filaments, there is a single, *discontinuous* unbinding transition, see Figure 6(a). In the presence of a hard-core repulsion, the critical potential strength $\bar{W}_\mathrm{c}$ saturates to a N-independent limiting value $\bar{W}_{\mathrm{c},\infty}$ for large N. The numerical simulations support a scaling behavior $\bar{W}_{c,\infty} - \bar{W}_c \sim N^{-\lambda}$ with an exponent $\lambda \simeq 1.0 \pm 0.1$ as shown in Figure 7. As can be seen in Figure 4(a) typical bundle morphologies close to the transition are governed by pair contacts of filaments. The bundle thickness, as given by the mean segment separation $\langle|\Delta\mathbf{z}_{ij}| - \ell_r\rangle$, stays *finite* up to the transition, see MC data in Figure 6(b). For increasing N, an increasing number of higher moments $\langle(|\Delta\mathbf{z}_{ij}| - \ell_r)^m\rangle$ remains finite at the

[†]This corrects the corresponding Eqs. in Ref. [5]; The effective interaction $\bar{\mathcal{H}}_2$ contains an additional factor 1/2, and the effective potential strength $\bar{W}$ an additional factor 2.

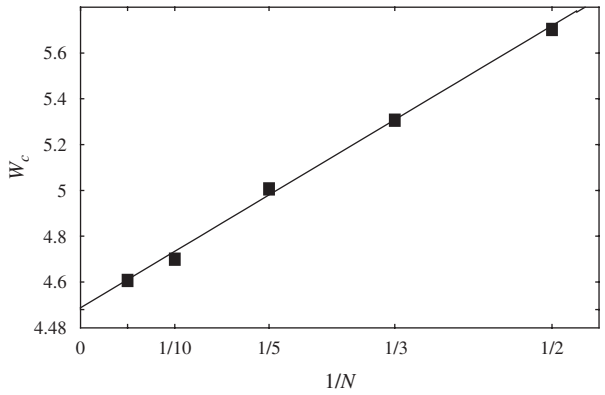

Fig. 7. MC data points for the critical potential strength $|W_c|$ as a function of the inverse filament number $1/N$. The data points are fitted well by a straight line with a limiting value $\overline{W}_{c,\infty} \simeq 4.48$.

transition (all moments $m < 2(N-1)(3N-4)/3$ remain finite) showing that the critical thickness fluctuations of large bundles become small.

Deep in the bundled phase, i.e., for large $|\overline{W}|$, our MC simulations show that bundles do not always reach their equilibrium shape. Small sub-bundles containing typically $N \sim 5$ filaments form easily, start to entangle, and further equilibration is kinetically trapped suggesting that the bundle is in a "glass" phase. Figure 4(b) shows the segregation into sub-bundles in a typical configuration and Figure 6(a) shows the corresponding rise in the mean bundle energy per filament which approaches the $N = 5$ result. In Figure 6(b) the pronounced rise of the mean separation for $N > 5$ with increasing potential strength and with increasing N is due to the segregation. This behavior is reminiscent of the experimentally observed F-actin structures consisting of networks of small bundles.[11] Only when starting from a sufficiently compact initial state, bundles relax towards the equilibrium form in the MC simulation, which is a roughly cylindrical bundle with a hexagonal filament arrangement as shown in Figure 4(c). In contrast to the segregated form, the bundle thickness and the mean energy per filament of the equilibrium form decrease with increasing N, as can be seen in Figure 6.

The critical potential strength $\overline{W}_c$ corresponds to a critical crosslinker concentration $X_{1,c}$. For weakly bound linkers $|W| \ll T/a_\parallel$, we have a simple linear relation $\overline{W} \approx 2X_1 W$ such that $X_{1,c} \approx \overline{W}_c/2W$. The corresponding relation for strongly bound linkers is more complicated but $X_{1,c}$ will increase monotonically with increasing $\overline{W}_c$.

Our simulations use periodic boundary conditions and treat very long and essentially parallel filaments. In order to include translational and rotational entropy we can map the ensemble of semiflexible filaments considered here onto an ensemble of rigid rods of finite length L and diameter $a_\perp$ at a certain concentration c. The effective pairwise attraction (per length) J is given by the bundling free energy of the filaments with $J \sim \overline{W}_c - \overline{W} > 0$ for $|\overline{W}| > |\overline{W}_c|$. Using the results of Ref. [32], we find that the hard rod system separates into a high-density nematic phase and a low-density nematic or isotropic phase above a critical attraction, which is in qualitative agreement with the experimental results in Refs. [10–12].

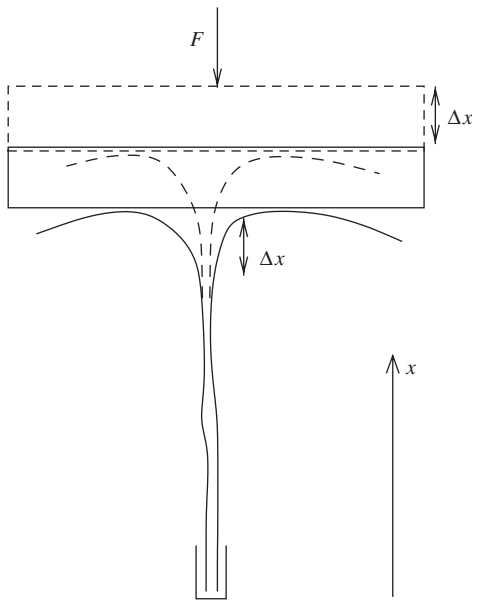

Fig. 8. Schematic illustration of the zipping mechanism. Upon zipping or bundling of filaments over an additional length Δx they gain an adhesion energy $J\Delta x$. Motion of the wall over the same distance Δx against an external force f requires an energy $f\Delta x$.

4.3. Force-Generation by Bundling or Zipping

The adhesive energy which is gained during bundle formation can be used to generate forces. The basic mechanism can be explained for two filaments which are bundling or zipping due to a short-range attraction as discussed in the previous section. As sketched in Figure 8, we start with a bundle of two filaments which is oriented in the x-direction. One end of the bundle—the lower end in Figure 8—is spatially fixed and has a clamped orientation. At the other end of the bundle—the upper end in Figure 8—the two filaments unbind and bend against a rigid wall. The wall exerts a total force F in the negative x-direction, such that each filament is loaded by a force $F/2$. As the filaments bind or zip together over an additional length Δx, they gain a free energy $J\Delta x$, where $J > 0$ is the free energy of adhesion (per length) as introduced in the previous section. In the absence of thermal shape fluctuations of the filaments, the free energy is equal to the energy of adhesion $J \approx |\overline{W}|$. In the presence of thermal fluctuations, this 'bare' adhesion energy is considerably reduced by entropic contributions until it finally vanishes as $J \sim \overline{W}_c - \overline{W}$ close to the unbundling transition as discussed above. Zipping together an additional length Δx implies that the wall moves by the same distance Δx which costs an energy $F\Delta x$. The total zipping free energy gain is $E_{zip} = (J - F)\Delta x$ and zipping happens spontaneously for

RESEARCH ARTICLE

forces f that satisfy

$$F < F_{\rm zip} = J \tag{19}$$

where $F_{\rm zip}$ is the maximal force which can be generated by this simple mechanism. Deep in the bundled phase, we have

$$F_{\rm zip} = J \approx |\bar{W}|, \quad \text{for } |\bar{W}| \gg |\bar{W}_{\rm c}| \tag{20}$$

The zipping mechanism does not rely on polymerization forces but requires a length reservoir for the filaments in front of the wall. This length reservoir has to be constantly renewed by polymerization at the free polymer ends as long as the zipping proceeds. Force generation by the zipping mechanism is eventually limited by the buckling instability of the bundled zipped stem. Similar zipping mechanisms have been proposed to play an essential role in the motility of nematode sperm cells.[33, 34]

We have performed MC simulations of the zipping mechanism for two identical filaments using an effective Hamiltonian

$$\mathcal{H} = \sum_i \mathcal{H}_{b,i} + \sum_{i,j} \bar{\mathcal{H}}_2$$

which we parameterize in terms of the contour length L of the filaments. Each filament is discretized into $L/\Delta s$ equidistant points along its contour. Initially, we prepare a bundle oriented in the x-direction parallel to the direction of the force with one end fixed and clamped, and the other end in a splayed configuration as shown in the snapshot Figure 9 on the left. During the MC simulation additional monomers can attach at the splayed ends (gaining a binding energy $E_m < 0$), which provides the necessary reservoir in polymer length. The wall is loaded with a force F and moved instantaneously (or adiabatically) to the monomer position with the largest x-coordinate after each MC step. After a steady state has established for a given force F we measure the mean velocity $\langle v_w \rangle$ of the pushing wall in the positive x-direction. In the MC simulations we find indeed a threshold behavior with a critical force $F_{\rm zip}$ in agreement with our argument above. At low pushing forces $F < F_{\rm zip}$, we find $\langle v_w \rangle > 0$, and the zipped part of the bundle is constantly growing, whereas at high forces $F > F_{\rm zip}$, it constantly shrinks since $\langle v_w \rangle < 0$. Our MC data are consistent with the above estimate (20) for $|\bar{W}| \gg |\bar{W}_{\rm c}|$, i.e., deep in the bundled phase, see Figure 9 on the right.

For bundles consisting of N filaments we expect the free energy gain from binding or zipping N filaments together over an additional length Δx to scale as $NqJ\Delta x/2$ for large N, where q is the number of nearest neighbors: Because of the repulsive part of their interaction, filaments in large bundles only interact with a limited number q of nearest neighbors for short-range attractions. Moving the wall by the same distance Δx costs an energy $F\Delta x$ and, thus, we expect $F_{\rm zip} \sim NqJ/2$ for the maximal force that can be generated by the zipping of a bundle consisting of a large number N of filaments.

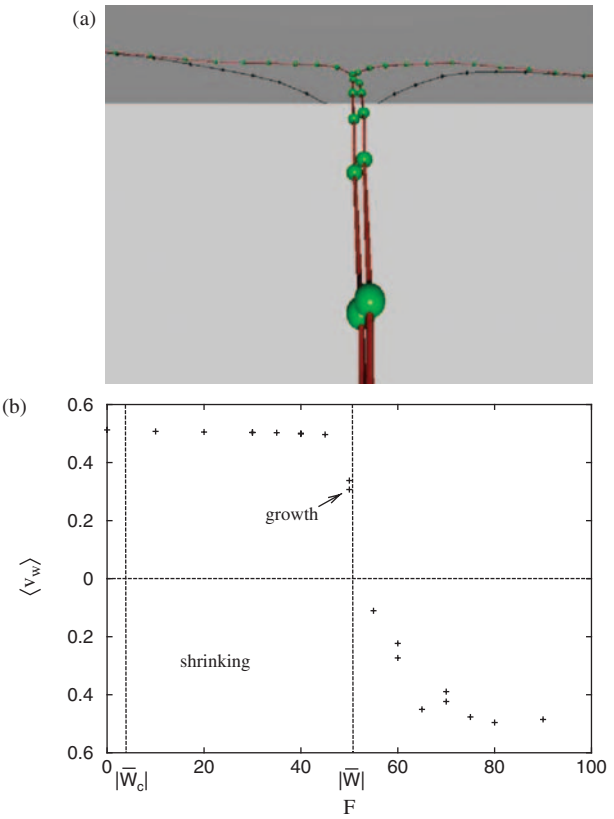

Fig. 9. (a) Snapshot from MC simulations of zipping for two polymers with $L_{\rm p} = 2000$ (in units of Δs), an adhesive potential of $|\bar{W}| = 50$, and a force $F = 50$ (both in units of $T/\Delta s$), i.e., close to the critical force $F_{\rm zip}$. The wall is visible in dark grey, the immobilized clamped ends of the filaments are outside the range of the picture in the front. (b) Mean velocity $\langle v_w \rangle$ (in units of Δs per MC time step) of the pushing wall for an adhesive potential with $|\bar{W}| = 50$ as a function of the pushing force F. The other parameters are as in Figure 6; the critical potential strength for bundling is $|\bar{W}_{\rm c}| \simeq 3.2$, i.e., the simulations are performed deep in the bundled phase. The arrow corresponds to the snapshot on the left. For $F < F_{\rm zip}$ we find $\langle v_w \rangle > 0$, and the zipped part of the bundle is growing. For $F > F_{\rm zip}$, it shrinks and $\langle v_w \rangle < 0$. The MC data is consistent with $F_{\rm zip} \approx |\bar{W}| = 50$, see (20).

5. FILAMENT ADSORPTION

The adsorption transition of a single filament onto a planar substrate is qualitatively similar to the bundle formation for $N = 2$ filaments in $1+1$ dimensions, where the one-dimensional perpendicular distance $z(x)$ from the surface is analogous to a one-dimensional separation between filaments. The adsorption transition can be solved analytically,[15] which reveals that unbinding and desorption represent two distinct universality classes with different critical exponents.

Here we want to consider the adsorption of a filament with persistence length $L_{\rm p} = 2\kappa/T$ on a planar two-dimensional substrate where molecular motors are adsorbed with an areal density σ. Each motor can bind to a filament within a capture radius ℓ_m and a binding energy $W_m < 0$. Then each motor gives rise to an adsorption

potential $V_{\rm ad}(z)$ of the same functional form as the potential (17),

$$V_{\rm ad}(z) = W_m \quad \text{for } 0 < z < \ell_m \quad \text{and} \quad V_{ad}(z) = 0 \text{ otherwise} \tag{21}$$

In the following we assume that the motor tail is flexible such that the filament can bind at any orientation. A rigid motor tail eventually gives rise to an orientation-dependent adsorption potential because filaments could bind only at a preferred angle. In Ref. [15] both cases have been discussed, and it has been found that the orientation-dependence can affect the order of the adsorption transition. Whereas we find for orientation-independent adsorption potentials a second order transition, the adsorption transition can become first order if the potential is orientation-dependent.[‡] In contrast to the case of the annealed crosslinker ensemble considered previously, the motors represent a partially *quenched* ensemble of adsorption points. In the following, we consider the typical experimental situation of a rather uniform coverage with motor proteins and also neglect effects from filament fluctuations parallel to the surface. Then the array of motors gives rise to an average adsorption potential $\overline{V}_{\rm ad}(z)$ of the same functional form as the potential (21) with a potential strength $\overline{W}_{\rm ad} = W_m \sigma \ell_m$. On length scales comparable or smaller than $L_{\rm p}$, the semiflexible polymer is only weakly bent by thermal fluctuations and its configurations are governed by the effective Hamiltonian

$$\mathcal{H}_{\rm ad} = \int_0^{L_\parallel} dx \left[\frac{\kappa}{2} (\partial_x^2 z)^2 + \overline{V}_{\rm ad}(z(x)) \right] \tag{22}$$

We consider the limit of long filaments $L_\parallel \overline{W}_{\rm ad} \gg T$, which can exhibit a desorption transition. Using the model (22), this desorption transition has been studied by transfer matrix techniques in Ref. [15]. The critical potential strength for desorption is $\overline{W}_{{\rm ad},\,c} = -cT\ell_m^{-2/3} L_{\rm p}^{-1/3}$ corresponding to a critical motor density

$$\sigma_c = c \frac{T}{W_m \ell_m^{5/3} L_{\rm p}^{1/3}} \tag{23}$$

where $c \approx \sqrt{3\pi}/2 \approx 1.5$. For motor densities above the critical density, filaments adsorb onto the substrate with anchored motors against the thermal fluctuations of filaments. The critical motor density for adsorption is decreasing with increasing filament rigidity κ. Using estimates $W_m \simeq 15T$ and $\ell_m \simeq 10^{-2}$ μm for kinesin and $L_{\rm p} \simeq 10$ mm for microtubules, we find a critical motor density $\sigma_c \simeq 10$ $\mu{\rm m}^{-2}$ for adsorption.

The transfer matrix treatment shows that the free energy difference between adsorbed and unbound state vanishes as $|\Delta f| \approx |\overline{W}_{{\rm ad},\,c}||w|/\ln|w|^{-1}$ where $w \equiv (\overline{W}_{\rm ad} - \overline{W}_{{\rm ad},\,c})/\overline{W}_{ad,\,c}$. Therefore, the correlation length $\xi_\parallel = T/|\Delta f| \propto |w|^{-\nu}$ diverges with an exponent $\nu = 1 + \log$. The weak bending approximation is valid as long as gradients are small, i.e., $\langle (\partial_x z)^2 \rangle \sim \xi_\parallel / L_{\rm p} \lesssim 1$, which is fulfilled for $|\overline{W}_{\rm ad} - \overline{W}_{{\rm ad},\,c}| \gtrsim T/L_{\rm p}$, which typically applies to stiff filaments such as microtubules adsorbed by kinesins.

[‡]The case of an orientation-independent adsorption potential (21) corresponds to the case $\Delta = 0$ in Ref. [15].

6. MOTILITY ASSAYS FOR MOTOR PROTEINS

Motility assays are model systems, which allow to study active filament dynamics in a controlled manner. In motility assays, filaments are connected to the substrate by anchored motors of sufficient density $\sigma > \sigma_c$. In the presence of ATP, the motor heads start to perform a directed walk on the filaments, which induces active dynamics of adsorbed filaments. By analyzing the transport velocities of single filaments gliding over the substrate, information can be obtained about basic properties of molecular motors such as their maximal velocity. If many interacting filaments are studied interesting active ordering phenomena can occur.

6.1. Model

Our microscopic model for motility assays describes filaments, motor heads, and polymeric motor tails as separate degrees of freedom.[25] One end of the motor tail is anchored to the substrate and the motor head on the other end can bind to a filament with the correct orientation since the motor tail is rather flexible. Once bound the motor head moves along the filament thereby stretching the polymeric tail, which gives rise to a loading force acting both on the motor head and the attached filament. This force feeds back onto the motion of the bound motor head, which moves with a load-dependent motor velocity.[35, 36] Filaments follow an overdamped dynamics with external forces arising from the stretched motor tails and the repulsive filament–filament interaction.

To proceed, let us consider N rigid filaments of length L on a planar two-dimensional substrate.[¶] The configuration of filament i ($i = 1, \ldots, N$) is then specified by the position of its center of mass $\mathbf{r}_i$ and its orientation angle θ_i, see Figure 10. The overdamped translational and rotational dynamics of each filament i is described by the stochastic Langevin-type equations of motion[25]

$$\mathbf{\Gamma} \cdot \partial_t \mathbf{r}_i = \sum_{\alpha=1}^{N_i} \mathbf{F}_i^\alpha \sum_{j=1}^{N} \mathbf{F}_{ij} - \boldsymbol{\zeta}_i \tag{24}$$

and

$$\Gamma_\theta \partial_t \theta_i = \sum_{\alpha=1}^{N_i} M_i^\alpha + \sum_{j=1}^{N} M_{ij} + \zeta_{\theta,\,i} \tag{25}$$

where N_i is the number of motor heads attached to filament i and indexed by α. The vector $\mathbf{u}_i = (\cos\theta_i, \sin\theta_i)$ is

[¶]The model can be extended to deformable filaments by modeling each filament as a set of N_s segments connected by elastic springs and hinges, see P. Kraikivski, Ph.D. Thesis, Universität Potsdam (2005).

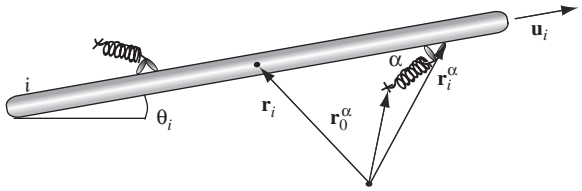

Fig. 10. Schematic view onto substrate surface: A filament i attached by two motors attached. The vector $\mathbf{r}_i$ points towards the filament's center of mass, the parameters θ_i and $\mathbf{u}_i$ represent the orientational angle and unit vector, respectively. The motor α is anchored at $\mathbf{r}_0^\alpha$, and its head is positioned at $\mathbf{r}_i^\alpha$.

the orientational unit vector of filament i. Friction forces are governed by the matrix of translational friction coefficients, $\mathbf{\Gamma} = \Gamma_\parallel \mathbf{u}_i \otimes \mathbf{u}_i + \Gamma_\perp(\mathbf{I} - \mathbf{u}_i \otimes \mathbf{u}_i)$,[21] where $\mathbf{I}$ is the unit matrix and Γ_θ is the rotational friction coefficient. All friction coefficients $\Gamma_\parallel$, $\Gamma_\perp$, and Γ_θ are known from passive filament dynamics. The translational and angular thermal random forces $\boldsymbol{\zeta}_i(t)$ and $\zeta_{\theta,i}(t)$, respectively, are Gaussian distributed with correlations $\langle \boldsymbol{\zeta}_i(t) \otimes \boldsymbol{\zeta}_j(t') \rangle = 2T\mathbf{\Gamma}\delta_{ij}\delta(t-t')$ and $\langle \zeta_{\theta,i}(t)\zeta_{\theta,j}(t') \rangle = 2T\Gamma_\theta\delta_{ij}\delta(t-t')$. The stretched tail motor α is exerting a force $\mathbf{F}_i^\alpha$ onto the filament. The end-to-end vector of the polymeric tail is $\Delta\mathbf{r}^\alpha \equiv \mathbf{r}_i^\alpha - \mathbf{r}_0^\alpha$, where the motor tail is anchored at $\mathbf{r}_0^\alpha$ and the head position is $\mathbf{r}_i^\alpha$. We model the polymeric tail as freely jointed chain such that $\mathbf{F}_i^\alpha$ is pointing in the direction $-\Delta\mathbf{r}^\alpha$ and its absolute value is obtained by inverting the force-extension relation of a freely jointed chain.[26] There is also a corresponding torque due to the motor activity, $M_i^\alpha = |(\mathbf{r}_i^\alpha - \mathbf{r}_i) \times \mathbf{F}_i^\alpha|$. The interaction forces $\mathbf{F}_{ij}$ and torques M_{ij} are due to the purely repulsive interactions between filaments i and j corresponding to a hard-rod interaction for filaments of diameter D.

The dynamics of motor heads is described by a deterministic equation of motion, which has the form

$$\partial_t x_i^\alpha = v(\mathbf{F}_i^\alpha) \tag{26}$$

where $|x_i^\alpha| \le L/2$ defines the position of the motor α on the rod i, i.e., $\mathbf{r}_i^\alpha = \mathbf{r}_i + x_i^\alpha \mathbf{u}_i$ and the filament polarity is such that the motor head moves in the direction $\mathbf{u}_i$. The motor velocity v is a function of the loading force $\mathbf{F}_i^\alpha$ which builds up as the motor tail becomes more and more stretched. We use a piecewise linear force-velocity relation

$$\begin{aligned} v(\mathbf{F}_i^\alpha) &= v_{\max} \quad \text{for } \mathbf{F}_i^\alpha \cdot \mathbf{u}_i \ge 0 \\ &= v_{\max}\left(1 - \frac{|\mathbf{F}_i^\alpha|}{F_{\rm st}}\right) \quad \text{for } \mathbf{F}_i^\alpha \cdot \mathbf{u}_i < 0 \quad \text{and} \quad |\mathbf{F}_i^\alpha| < F_{\rm st} \\ &= 0 \quad \text{for } \mathbf{F}_i^\alpha \cdot \mathbf{u}_i < 0 \quad \text{and} \quad |\mathbf{F}_i^\alpha| > F_{\rm st} \end{aligned} \tag{27}$$

where $v_{\max}$ is the maximal motor velocity, which is attained if the motor is pulled forward. The motor speed decreases linearly if the motor is pulled backwards, until it stalls if the backwards force exceeds the stall force $F_{\rm st}$.[35,36] We assume that the motor binds to the filament when the distance between the position of the fixed end of the motor tail at $\mathbf{r}_0^\alpha$ and the filament is smaller than the capture radius ℓ_m. Apart from the stall force $F_{\rm st}$ the motor is also characterized by its detachment force $F_{\rm d}$, above which the unbinding rate of the motor head becomes large. For simplicity we assume in our model that the motor head detaches whenever the force F_i^α exceeds a threshold value $F_{\rm d}$. We consider the case of processive motors with a high duty ratio close to unity, i.e., motors detach from a filament only if they reach the filament end or if the force F becomes larger than the detachment force $F_{\rm d}$.

6.2. Simulation

Using the above model we can perform simulations of gliding assays for different distributions of motors, i.e., random distributions or patterns of motors. We will first focus on a random distribution of motors with a surface density σ and a system with periodic boundary conditions. At each time step Δt, we update the motor head position x_i^α and filament position by using the discrete version of the equations of motion (25) and (26). The parameter values that we choose for the simulations are comparable with experimental data on assays for conventional kinesin. The simulation results presented in this article have been obtained for assays of quadratic geometry and area 25 μm^2 with rigid filaments of length $L = 1$ μm and diameter $D = L/40$. We simulate at room temperature $T = 4.28 \times 10^{-3}$ pN μm. The friction coefficients are taken to be $\Gamma_\perp = 2\Gamma_\parallel = 4\pi\eta L/\ln(L/D)$ and $\Gamma_\theta = \Gamma_\parallel L^2/6$, where η is the viscosity of the surrounding liquid. We use a value $\eta = 0.5$ pN s/μm^2 much higher than the viscosity of water, $\eta_{\rm water} \sim 10^{-3}$ pN s/μm^2, which allows to take larger time steps and decreases the simulation time. We checked that this does not affect results by performing selected simulation runs also at the viscosity of water. We use a maximum motor speed of $v_{\max} = 1$ μm s^{-1} and a stall force of $F_{\rm st} = 5$ pN. The capture radius for motor proteins is $\ell_m = 10^{-2}$ μm and the length of the fully stretched motor tail $L_m = 5 \times 10^{-2}$ μm.

The motion of a *single* filament with contour length L is characterized by stochastic switching between rotational and translational diffusion if no motors are attached, directed translation in rotationally diffusing directions if one motor is attached, and directed translation in one direction if two or more motors are attached. The relative frequency of these types of motion depends on the average number of motors attached to the filament or the average distance $\langle d_m \rangle$ between bound motors and, thus, on the surface motor concentration σ.[22] In the limit of high motor concentration a filament has two or more bound motors on average and $\langle d_m \rangle \sim 1/\sigma\ell_m$. The single filament performs a persistent walk with the effective persistence length[22]

$$\xi_{\rm p} = \frac{\langle S_\theta \rangle}{\langle \Delta\theta^2 \rangle^{1/2}} = \frac{L + 2\langle d_m \rangle}{L + 3\langle d_m \rangle} \frac{L^3}{9\ell_m^2} \left(e^{L/\langle d_m \rangle} - 1 - \frac{L}{\langle d_m \rangle} \right) \tag{28}$$

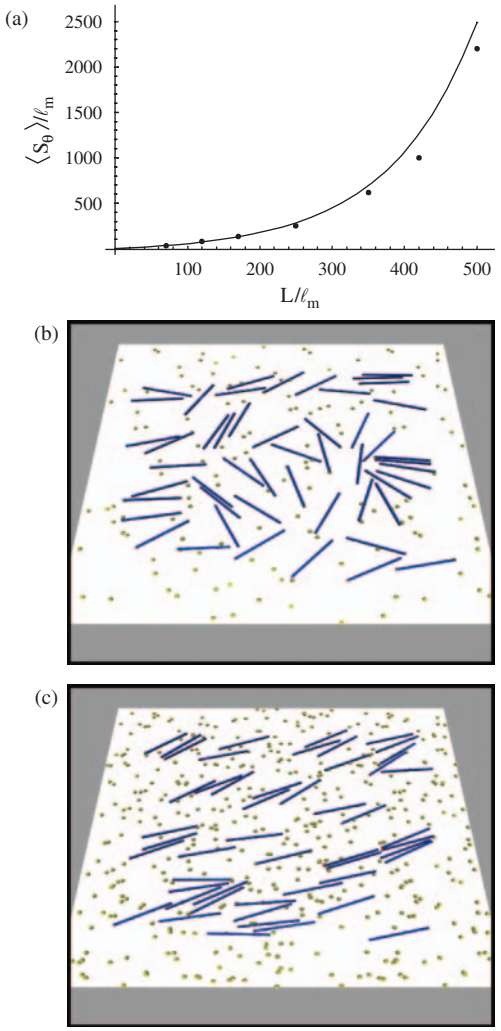

Fig. 11. (a) Simulation results for average distance $\langle S_\theta \rangle$ traveled by a filament between successive rotations as a function of the filament length L for high motor concentration. The solid line is the analytical result (28) as derived in Ref. [22]. (b) and (c) Snapshots of a gliding assay of rod-like filaments with filaments density $\rho = 2/L^2$ on a motor coated substrate with randomly distributed motors and periodic boundary conditions. For detachment forces $F_d = F_{st}$, we find (b) an isotropic phase at low motor surface density $\sigma \ell_m L = 0.03$ and (c) active nematic ordering at high motor surface density $\sigma \ell_m L = 0.09$.

where $\langle S_\theta \rangle$ is the average distance traveled by a filament between successive rotations and $\langle \Delta\theta^2 \rangle^{1/2} = 3/\sigma L^2$ is the average rotation angle at each rotation. The theoretical result (28) is confirmed by our simulation as shown in Figure 11(a). The average filament velocity $v_F = \langle |\dot{\mathbf{r}}_i| \rangle$ can be obtained by simultaneously equating (i) the filament friction force with the total motor driving force and (ii) the filament velocity with the motor velocity in the steady state, which leads to $v_F = v_{max}(1 + \Gamma_\parallel v_{max} \langle d_m \rangle / L F_{st})^{-1}$. This relation is confirmed by our simulations.

6.3. Enhanced Ordering

Our results for the simulation of *many* filaments with hard-core interactions indicate that the motility assay

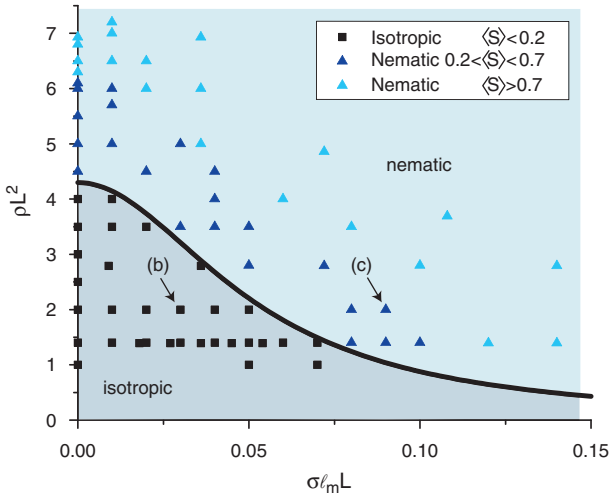

Fig. 12. The phase diagram of the gliding assay as a function of the dimensionless filament density ρL^2 and dimensionless surface motor density $\sigma \ell_m L$ for a detachment force $F_d = F_{st}$ and $L/\ell_m = 100$. Each simulation run corresponds to one data point; arrows correspond to the snapshots in Figure 11. If the average order parameter $\langle S \rangle < 0.2$, the system is in the isotropic phase (black squares, grey area), if $\langle S \rangle > 0.2$ it is in the nematic phase (blue triangles, blue area). The solid line represents the analytical result (30).

exhibits *active nematic ordering* if the motor density σ is increased as can be seen in the two simulation snapshots Figures 11(b) and (c).[25] Both the rod density ρ and the motor density σ are essential in order to determine the phase behavior of the non-equilibrium motility assay. For given L/ℓ_m, the corresponding phase diagram depends on the dimensionless which can be described in the plane of the two dimensionless parameters ρL^2 and $\sigma \ell_m L$ as shown in Figure 12. Nematic ordering in a system of N filaments can be characterized by the time averages of the order parameter $S \equiv \sum_{i \neq j} \cos(2(\theta_i - \theta_j))/N(N-1)$. In equilibrium, i.e., in the absence of motors ($\sigma = 0$) we find a continuous isotropic-nematic transition at a critical density $\rho_{c,0} \simeq 4.3/L^2$ in the simulation, which is in good agreement with the analytic result $\rho_c = 3\pi/2L^2 \simeq 4.7/L^2$ based on Onsager's theory.[37] The equilibrium transition is found numerically from the inversion point of the curve $\langle S \rangle = \langle S \rangle(\rho)$ for a value $\langle S \rangle \simeq 0.2$, which we also use as the threshold value for active nematic ordering if motors are present and $\sigma > 0$, see Figure 12. Snapshots of the actively driven system in the isotropic and nematic phase are shown in Figures 11(b) and (c), respectively. In the resulting phase diagram in Figure 12, the critical density ρ_c for active nematic ordering *decreases* with increasing motor density, i.e., nematic ordering is favored if more mechanical energy is fed into the system. The transition is continuous also for non-zero motor-density. In the presence of motor activity, there is a non-vanishing filament current in the nematic phase, which is characteristic for a non-equilibrium phase. This filament current associated with the nematic order breaks the rotational symmetry and can be established only for periodic boundary conditions.

For a closed system with hard wall boundary conditions, on the other hand, we expect the formation of vortex-like rotating filament patterns.

The simulation results can be explained using the concept of an *effectively increased filament length*

$$L_{\mathrm{eff}} = \sqrt{L(L+\xi_{\mathrm{p}})} \tag{29}$$

as compared to the equilibrium system, which explains that motor activity actually favors nematic ordering. The increased effective length is an effect of the persistent motion of each filament, which effectively increases the excluded volume area. This concept can be derived more rigorously by coarse-graining in time and averaging over time intervals of one persistence time $t_{\mathrm{p}} = \xi_{\mathrm{p}}/v_{\mathrm{F}}$ in the framework of a dynamical mean-field approach. We finally obtain the critical filament density for the active isotropic-nematic transition,

$$\rho_{\mathrm{c}} = \frac{c}{L[L+\xi_{\mathrm{p}}(\langle d_m\rangle, \ell_m, L)]} \tag{30}$$

with $c = 3\pi/2$ from the analytical mean-field calculation. In the absence of motors we have $\xi_{\mathrm{p}} = 0$ and the relation (30) reduces to the equilibrium result of Ref. [37]. Using the expression (28) for the persistence length $\xi_{\mathrm{p}} = \xi_{\mathrm{p}}(\langle d_m\rangle, \ell_m, L)$, we obtain an explicit expression of the isotropic-nematic phase boundary in the active system in terms of the microscopic model parameters, which is in good agreement with the simulation data, see Figure 12. Beyond mean-field, we expect an increased numerical prefactor c in (30) but the same parameter dependence. For thermally fluctuating filaments the phase diagram in Figure 12 should be truncated for $\sigma < \sigma_{\mathrm{c}}$, see Eq. (23), where filaments can undergo thermal desorption from the planar substrate.

6.4. Filament Sorting

An interesting application of motility assays is filament size sorting or fractionation on the nanoscale using substrates coated with particularly designed *patterns* of molecular motor density. Using simple gradient patterns this possibility has already been explored experimentally in Ref. [38]. Here we propose a more efficient geometry and give a first proof of principle using our simulation model.

If there are two spatial regions I and II on the substrate, which are characterized by different motor densities σ_I and σ_{II} with $\sigma_{\mathrm{I}} < \sigma_{\mathrm{II}}$, filaments tend to move to region I of *low* motor density σ_{I}. If the substrate contains an alternating pattern of stripes of low and high motor density, as shown in Figure 13, the filaments accumulate in the stripes with low motor density, unless the width L_σ of the stripes of low motor density is larger than the filament length L. Then, filaments can "bridge" the stripes of low motor density. This behavior can be used to construct an assay for the sorting of filaments according to their lengths by patterning the substrate with low motor density stripes which are arranged with *increasing* width as shown in Figure 13 for three stripes. In general we can sort filaments into N_σ stripes with widths $L_{\sigma,1} < L_{\sigma,2} < \cdots < L_{\sigma,N_\sigma}$. A filaments of length L can bridge all narrow stripes until it encounters a stripe s with $L_{\sigma,s-1} < L < L_{\sigma,s}$, which is sufficiently broad to "trap" the filament. Figure 13 demonstrates that this sorting principle works for an assay consisting of a ternary mixture of filaments.

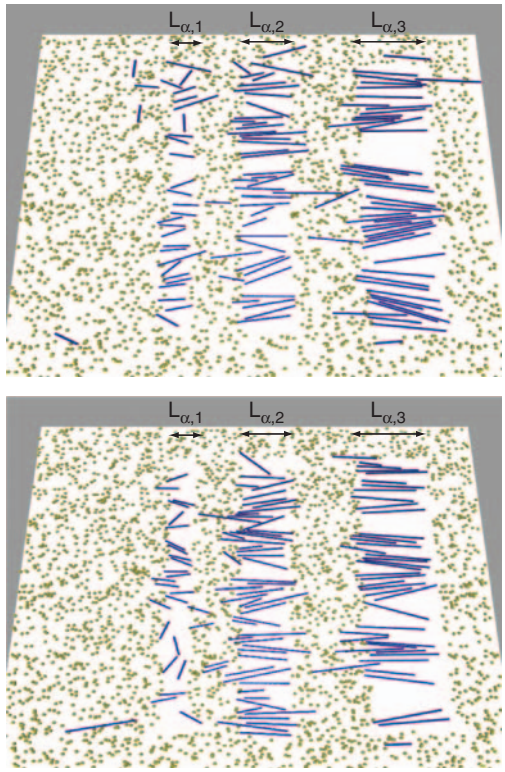

Fig. 13. Snapshots of gliding assays of a ternary mixture of rod-like filaments of different lengths on a substrate coated with an alternating pattern of stripes of low ($\sigma_1 = 0$) and high ($\sigma_2 > 0$) motor density. Each system of area 96.3 μm^2 contains a ternary mixture of $N = 120$ filaments with 40 filaments of length $L_1 = 0.5$ μm, $L_2 = 1$ μm, and $L_3 = 1.4$ μm each, which corresponds to a total filament density of $\rho L_2^2 = 1.25$. The stripes have increasing width from left to right with $L_{\sigma,1}/L_1 = 0.58$, $L_{\sigma,2}/L_1 = 1.165$, and $L_{\sigma,3}/L_1 = 1.73$. The motor density σ_2 outside the stripes is high with $\sigma_2 \ell_m L_2 = 0.24$ for the assay (a) and $\sigma_2 \ell_m L_2 = 0.3$ for (b). Both snapshots clearly indicate the sorting of filaments according to their lengths within the different stripes.

7. CONCLUSION AND OUTLOOK

Semiflexible polymers and filaments, which are ubiquitous both in natural biological systems and synthetic biomimetic chemical systems, are nanorods which are subject to thermal fluctuations and external forces. In this review we covered some of the cooperative phenomena that can arise from the presence of a large number of internal bending modes or by interactions in filament assemblies.

We discussed the persistence length of a single filament using a renormalization group approach and some

characteristics of the buckling instability of a single filament. Then we moved on to systems containing ensembles of filaments and presented simulations and analytical results for bundling transitions, which can also be used to generate forces on the nanoscale by means of zipping mechanisms. Finally we presented a simulation model for motility assays where filaments are subject to active fluctuations from motor proteins that are immobilized on a substrate. This active driving leads to an enhanced tendency for nematic ordering.

In this review, we focused on thermally fluctuating biological filaments. Principles which are realized in nature can guide the design of artificial or synthetic devices, which fulfill similar tasks as their biological counterparts. One particularly interesting example might be force generation on the nanoscale, where nature uses polymerizing or zipping forces which could be imitated in synthetic or biomimetic polymer systems in the future. Another example where experimental work has already started are size sorting assays for the fractionation of filaments.[38] For synthetic metal nanorods, also quantum fluctuations might play a role in future experiments (see Ref. [39] for an example), which have not been discussed in this review.

Acknowledgments: This work was supported by the EC Sixth Framework Programme (as part of the STREP Active Biomics contract No. NMP4-CT-2004-516989).

LIST OF SYMBOLS

c_x	crosslinker conc. in solution
D	filament diameter
$\langle d_m \rangle$	mean distance between bound motors
$\Delta \mathbf{r}^\alpha$	end-to-end vector of motor tail
κ	bending rigidity
ℓ	RG length scale
ℓ_b	bond length
ℓ_a	range of linker potential
ℓ_m	motor capture radius
ℓ_r	hard core size
η	viscosity of the surrounding liquid
F	compressional force
F_c	critical force for buckling
F_d	detachment force
$\mathbf{F}_i^\alpha$	loading force onto filament i from motor head α
$\mathbf{F}_{ij}$	filament interaction forces
F_{st}	stall force
F_{zip}	maximal zipping force
$\Gamma_\parallel$, $\Gamma_\perp$	filament friction coefficients
Γ_θ	rotational friction coefficient
$\phi(s)$	tangent angles
J	free energy of adhesion
L	filament contour length
$L_\parallel$	filament projected length
L_c	critical length for buckling
L_{eff}	effective filament length (29)
L_p	persistence length (4)
L_σ	width of stripe of low motor density
M	bond number
M_i^α	torque onto filament i from motor head α
M_{ij}	filament interaction torques
$n_{i,k}$	crosslinker occupation on site k of filament i
N	number of filaments in a bundle or assay
N_σ	number of stripes
$\mathbf{r}_i$	center of mass of filament i
$\mathbf{r}_0^\alpha$	anchor point of tail of motor α
$\mathbf{r}_i^\alpha$	position of head of motor α on filament i
R	RG step number
ρ	filament density
ρ_c	critical filament density for ordering
s	arc length
S	nematic order parameter
$\langle S_\theta \rangle$	mean distance traveled by a filament between rotations
σ	motor density
$\mathbf{t}$	tangent vector
t	time
t_p	persistence time of filament motion
T	temperature (in energy units)
θ_i	angle of filament i
$\mathbf{u}_i$	orientation of filament i
v_F	mean filament velocity
v_{max}	maximal motor velocity
$\langle v_w \rangle$	mean zipping velocity
$V_a(\mathbf{z})$	linker-mediated potential (17)
$V_{ad}(z)$	adsorption potential (21)
$V_r(\mathbf{z})$	hard-core repulsion
W	adhesive energy (per length) of one linker end group
$\bar{W}$	effective potential strength (18)
W_m	motor binding energy
$\bar{W}_{ad}$	effective adsorption potential strength
$\bar{W}_c$	critical potential strength for bundling
x	1-dim. coordinate parallel to filament
x_i^α	position of motor α on filament i
X_1	crosslinker conc. per filament site
$X_{1,c}$	critical crosslinker conc. per site for bundling
ξ_p	persistence length of filament motion (28)
$\mathbf{z}$	$(d-1)$-dim. coordinate perp. to filament
$\boldsymbol{\zeta}_i(t)$	translational thermal random force
$\zeta_{\theta,i}(t)$	rotational thermal random torque

References

1. D. Bray, Cell Movements: From Molecules to Motility, Garland Publishers (**2001**).
2. J. Howard, Mechanics of Motor Proteins and the Cytoskeleton, Sinauer Associates, Inc. (**2001**).
3. C. Ecker, N. Severin, L. Shu, A. D. Schlüter, and J. P. Rabe, *Macromolecules* 37, 2484 (**2004**).
4. P. Gutjahr, R. Lipowsky, and J. Kierfeld (unpublished).

RESEARCH ARTICLE

5. J. Kierfeld, T. Kühne, and R. Lipowsky, *Phys. Rev. Lett.* 95, 038102 **(2005)**.
6. A. Ott, M. Magnasco, A. Simon, and A. Libchaber, *Phys. Rev. E* 48, R1642 **(1993)**; J. Käs, H. Strey, and E. Sackmann, *Nature* 368, 226 **(1994)**.
7. F. Gittes, B. Mickey, J. Nettleton, and J. Howard, *J. Cell Biol.* 120, 923 **(1993)**.
8. J. R. Bartles, *Curr. Opin. Cell Biol.* 12, 72 **(2000)**.
9. K. R. Ayscough, *Curr. Opin. Cell Biol.* 10, 102 **(1998)**; S. J. Winder, *Curr. Opin. Cell Biol.* 15, 14 **(2003)**.
10. M. Tempel, G. Isenberg, and E. Sackmann, *Phys. Rev. E* 54, 1802 **(1996)**.
11. O. Pelletier, E. Pokidyshevam, L. S. Hirst, N. Bouxsein, Y. Li, and C. R. Safinya, *Phys. Rev. Lett.* 91, 148102 **(2003)**.
12. M. L. Gardel, J. H. Shin, F. C. MacKintosh, L. Mahadevan, P. Matsudaira, and D. A. Weitz, *Science* 304, 1301 **(2004)**.
13. D. Pantaloni, C. Le Clainche, and M.-F. Carlier, *Science* 292, 1502 **(2001)**.
14. A. Mogilner and G. Oster, *Curr. Biol.* 13, R721 **(2003)**.
15. J. Kierfeld and R. Lipowsky, *Europhys. Lett.* 62, 285 **(2003)**; J. Kierfeld and R. Lipowsky, *J. Phys. A: Math. Gen.* 38, L155 **(2005)**.
16. S. S. Sheiko and M. Möller, *Chem. Rev.* 101, 4099 **(2001)**.
17. N. Severin, J. Barner, A. A. Kalachev, and J. P. Rabe, *Nano Lett.* 4, 577 **(2004)**.
18. P. Kraikivski, R. Lipowsky, and J. Kierfeld, *Europhys. Lett.* 66, 763 **(2004)**; P. Kraikivski, R. Lipowsky, and J. Kierfeld, *Eur. Phys. J. E* 16, 319 **(2005)**.
19. P. Kraikivski, R. Lipowsky, and J. Kierfeld, *Europhys. Lett.* 71, 138 **(2005)**.
20. J. Scholey, Motility assays for motor proteins. Methods in Cell Biology, Academic Press **(1993)**, p. 39.
21. M. Doi and S. F. Edwards, The Theory of Polymer Dynamics, Clarendon **(1986)**.
22. T. Duke, T. E. Holy, and S. Leibler, *Phys. Rev. Lett.* 74, 330 **(1995)**.
23. M. R. Faretta and B. Basetti, *Europhys. Lett.* 41, 689 **(1998)**.
24. F. Gibbons, J.-F. Chauwin, M. Despósito, and J. V. Joseé, *Biophys. J.* 80, 2515 **(2001)**.
25. P. Kraikivski, R. Lipowsky, and J. Kierfeld, *Phys. Rev. Lett.* 96, 258103 **(2006)**.
26. J. Kierfeld, O. Niamploy, V. Sa-yakanit, and R. Lipowsky, *Eur. Phys. J. E* 14, 17 **(2004)**.
27. O. Kratky and G. Porod, *Rec. Trav. Chim.* 68, 1106 **(1949)**.
28. Th. Niemeijer and Th. W. Ruijgrok, *Physica* 81A, 427 **(1975)**.
29. M. Abramowitz and A. I. Stegun, Handbook of Mathematical Functions. *Natl. Bur. Stand.* **(1965)**.
30. L. D. Landau and E. M. Lifshitz, Theory of Elasticity, Pergamon **(1986)**.
31. S. Romero, C. Le Clainche, D. Didry, C. Egile, D. Pantaloni, and M.-F. Carlier, *Cell* 119, 419 **(2004)**.
32. M. Warner and P. J. Flory, *J. Chem. Phys.* 73, 6327 **(1980)**; A. R. Khokhlov and A. N. Semenov, *J. Stat. Phys.* 38, 161 **(1985)**.
33. A. Mogilner and G. Oster, *Science* 302, 1340 **(2003)**.
34. L. Miao, O. Vanderlinde, M. Stewart, and T. M. Roberts, *Science* 302, 1405 **(2003)**.
35. C. M. Coppin, D. W. Pierce, L. Hsu, and R. D. Vale, *Proc. Natl. Acad. Sci. USA* 94, 8539 **(1997)**.
36. S. M. Block, C. L. Asbury, J. W. Shaevitz, and M. J. Lang, *Proc. Natl. Acad. Sci. USA* 100, 2351 **(2003)**.
37. R. F. Kayser and H. J. Raveché, *Phys. Rev. A* 17, 2067 **(1978)**.
38. L. Ionov, M. Stamm, and S. Diez, *Nano Lett.* 5, 1910 **(2005)**.
39. H. B. Chan, V. A. Aksyuk, R. N. Kleiman, D. J. Bishop, and F. Capasso, *Science* 291, 1941 **(2001)**.

Received: 26 May 2006. Accepted: 18 July 2006.

RESEARCH ARTICLE